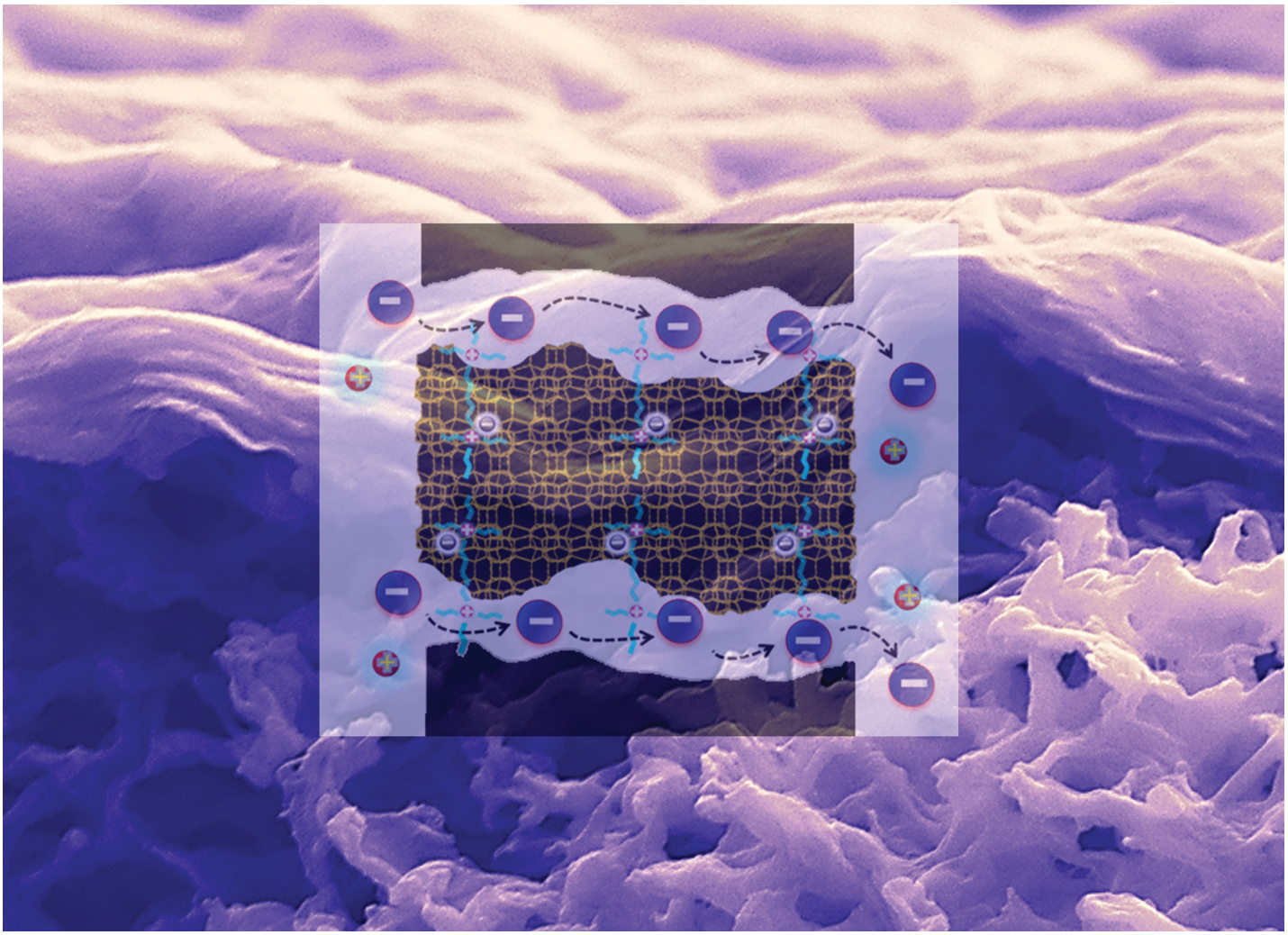

Showcasing research from Professor Dong's Membrane Laboratory, Department of Chemical and Environmental Engineering, University of Cincinnati, Cincinnati, Ohio, USA.

An anion exchange membrane of layered silicalite nanosheets with surface quaternary ammonium cations

Synthetic zeolite nanosheets with an enormous surface area and exposed quaternary ammonium cations of the template molecules are demonstrated as a new paradigm of building blocks for high-performance anion exchange membranes for electrochemical cells.

Image reproduced by permission of Junhang Dong, *Chem. Commun.*, 2025, **61**, 4503.

As featured in:

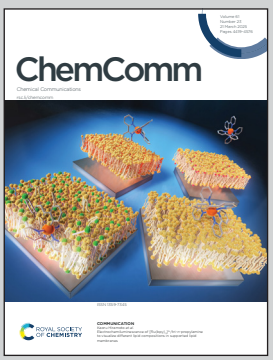

See Junhang Dong *et al.*, *Chem. Commun.*, 2025, **61**, 4503.

ROYAL SOCIETY OF CHEMISTRY

rsc.li/chemcomm

Registered charity number: 207890

ChemComm

COMMUNICATION

View Article Online
View Journal | View Issue

Cite this: *Chem. Commun.*, 2025, **61**, 4503

Received 24th December 2024,
Accepted 11th February 2025

DOI: 10.1039/d4cc06709f

rsc.li/chemcomm

An anion exchange membrane of layered silicalite nanosheets with surface quaternary ammonium cations†

Yukta Sharma, Devraj Singh, Zishu Cao,‡ Jan Gabski and Junhang Dong *

Silicalite nanosheets (SNs) with surfaced quaternary ammonium cations of the template molecules are demonstrated as a new paradigm of building blocks for anion exchange membranes (AEMs). A multilayered SN membrane is fabricated on porous PVDF to achieve 3 A cm^{-2} at 2.35 V and coulombic efficiency of 97% in alkaline water electrolysis.

AEM water electrolyzers (AEM-WEs) have great potential for cost-effective production of green hydrogen. To date, a few commercial AEMs have been tested for AEM-WEs, but none has been adopted by industry mainly because of their inadequate chemical stability and mechanical strength, large resistance, and high costs.[1] The development of AEMs has been largely focused on synthesizing new anion exchange polymers (AEPs) and innovating strategies for blending ionic and nonionic polymers to reduce the electrical resistance while enhancing the stability and mechanical resistance.[2] Some notable progress has been reported on the AEMs of aromatic ionic polymers such as the benzyl trimethylammonium, guanidinium, imidazolium, phosphonium, and metal–organic complex groups, *etc.*[3] In general, increasing the ionic group density in the AEP chains enhances the conductivity but reduces the mechanical stability and *vice versa* because the hydroxide ion (OH^-) attacks the carbon-backbone and the quaternary ammonium groups by intramolecular nucleophilic substitutions and Hoffman elimination. These destructive reactions are thermodynamically favored and worsen under low hydration.[4] Thus, improvement of AEM mechanical strength by blending AEPs with nonionic polymers is also limited because the latter reduces water uptake to decrease the stability and conductivity.[5]

Zeolites are crystalline aluminosilicates containing ordered pores of sizes ranging from 0.3 nm to over 1.0 nm depending on the crystallographic structures. The open-pore zeolite membranes have been demonstrated for proton-conduction while rejecting hydrated metal ions by size-exclusion in aqueous redox flow batteries (RFBs).[6] The membranes of MFI-type crystal structure (Fig. S1a and b, ESI†) are particularly desirable for proton conduction because of their excellent stability in both basic and acidic solutions and pore size ($\sim$0.56 nm) nearing the maximum for exclusion of hydrated metal ions (size $>$ 0.6 nm).[7] The recent success in the synthesis of MFI zeolite nanosheets (ZNs) has enabled ultrathin ZN-laminated membranes on polymer supports and mixed matrix membranes of preferentially aligned ZNs as proton conductors.[8,9] These ZN–polymer composite membranes can achieve high proton selectivity while reducing conduction resistance by shortening the proton transport pathways to enhance the efficiency of aqueous RFBs. However, the sub-nanometer zeolitic channels are unsuitable for anion transport due to strong steric hindrance.

Herein, we demonstrate the silicalite (pure-silica MFI) nanosheets (SNs) with surface quaternary ammonium cations (QAC) of the template molecules as a new type of anionic building block for high-performance AEMs. In this case, the zeolitic channels are occupied by diquaternary bis-1,5(tripropyl ammonium)pentamethylene diiodide (dC_5) molecules, which are templates directing the growth of SN.[10] The QAC groups of dC_5 are exposed at defects of incomplete cell structure (Fig. S1c and d, ESI†) that generate free OH^- by ionization in alkaline solutions, *i.e.*, $(\equiv N^+ \cdot OH^-)_{surface} \rightarrow (\equiv N^+)_{surface} + OH^-_{aqueous}$. An SN-layered membrane (SNLM) is coated on a porous PVDF substrate (SNLM–PVDF) and demonstrated for application as an efficient AEM for alkaline WE.

The SNs for membrane coating were obtained by epitaxial growth of two-unit cell-thick nanosheets from silicalite nanoparticle seeds using dC_5 as the template followed by extensive cleaning and mechanical removal of the seed-evolved cores (Fig. S2, ESI†).[11] The silicalite seeds with dia. $\sim$30 nm (Fig. S3a, ESI†) were synthesized by TPAOH-templated *in situ* crystallization.

Department of Chemical and Environmental Engineering, University of Cincinnati, Cincinnati, OH, 45221, USA. E-mail: dongj@ucmail.uc.edu

† Electronic supplementary information (ESI) available: SN synthesis procedure, AEM WE system and cell components, microscopic pictures of electrodes, membrane coating apparatus, strain–stress test results, and table of WE performance summary. See DOI: https://doi.org/10.1039/d4cc06709f

‡ Current address: Department of Chemical Engineering, University of Texas at Tyler, Tyler, TX 75799, USA.

The seeded growth of SN crystals used a precursor containing 80 TEOS : 3.75 dC_5 : 20 KOH : 9500 H_2O.[10,12] The resultant crystals were rhombus-shaped (Fig. S3b, ESI†) and were mechanically disintegrated to recover the flat SN flakes by sedimentation removal of the seed-evolved cores.[11]

The SNLM layer was formed on a porous PVDF film, which was selected for its thermal and chemical stabilities and commercial availability, by vacuum filtration coating (VFC, Fig. S4, ESI†) using a suspension containing 0.02 wt% SN and 0.06 wt% dissolved PVDF in a mixed solvent of 33 wt% DMSO and 67 wt% EtOH.[9,11] The VFC-coated SNLM–PVDF was immediately dried in a vacuum oven at 80 °C and ~1.5 kPa for 2 h and subsequently cured at 120 °C and ~24 kPa for 3 h. The PVDF binder intrinsically fused the SNLM layer with the PVDF substrate surface to create strong and stable adhesion.[9,11]

Characterization and tests. The SNs were examined by HR TEM and zeta potential (ζ) analysis in comparison with the SNs after dC_5 removal by firing in air at 550 °C for 6 h. The SNLM–PVDF membrane was examined by SEM, XRD, ATR-FTIR, and strain–stress test. The area-specific resistance (ASR) of the SNLM–PVDF was measured for various KOH solution concentrations (C_{KOH}) at different temperatures. A commercially obtained FAA3-50® (δ_m ~ 65 μm) AEM was parallelly tested. The EIS measurements and WE tests were performed using a system schematically shown in Fig. S5 (ESI†).

The membrane-electrode assembly (MEA) used 1 cm × 1 cm square electrodes, which were placed in the center of an AEM installed in the 2 cm × 2 cm gasket window (Fig. S5, ESI†). The anode was loaded with 2 mg cm^{-2} of a commercial $NiFe_2O_4$ catalyst (Thermo Scientific Chemicals) and the cathode was loaded with 0.5 mg cm^{-2} of a commercial Pt/C catalyst (Pt-Vulcan 40%, Fuel Cell Store), both coated on 1 cm × 1 cm Ni felts following the literature procedures (Fig. S6, ESI†). These electrodes were employed because of their reported good performance in AEM WE.[13,14] Photos of the actual electrodes are given in Fig. S5c (ESI†) and the SEM images of the electrodes are presented in Fig. S6 (ESI†). The KOH solutions were circulated at a flowrate of 20 mL min^{-1} on both sides. The performance of the WE cells equipped with the SNLM–PVDF and FAA3-50 AEMs were investigated by polarization curve measurements and stability tests in long-term WE using a 5 wt% KOH electrolyte.

SNs. The as-synthesized SN crystals were of typical rhombus shape (Fig. 1a) where the flat areas are known to have a uniform thickness of two unit-cells (*i.e.*, ~4 nm) in (010) orientation (*i.e.*, the *b*-direction of crystal cell).[10–12] The intensively cleaned flat SNs were highly perforated (Fig. 1b). The HR TEM images of the SNs revealed large numbers of surface defects (Fig. 1c) of incomplete zeolitic cells where the QAC groups of dC_5 are exposed for ionization upon hydration to enhance the anion conductivity. These lattice defects are the result of variations in crystal growth stage during the multicomponent multiphase reactions, which inevitably involve localized nonuniformity of reactant composition, temperature, and crystallization rates. The nonuniform crystallization is also the likely cause of holes in the SNs especially when the secondary growth is terminated prematurely within 4 days.[10,12] These holes are desirable for constructing the AEM because more defects and hence surface QACs exist in the edge areas. These holes also shorten the pathways for ion transport across the layered SNs by diffusion through the holes instead of along the entire SN surface.

The surface QAC-OH groups can be readily ionized in the KOH solution, *i.e.*, $(\equiv N^+ \cdot OH^-) \leftrightharpoons (\equiv N^+) + OH^-$. A suspension of dC_5-free SNs was also prepared after template removal.[11] The surfaced QAC groups ($\equiv N^+ \cdot OH^-$) in the nonactivated SN were evident by its significantly smaller ζ-potential (ζ = −16.00 ± 1.73 mV) as compared to the activated SNs (ζ = −31.92.0 ± 1.74 mV) in pure water (pH ~ 7.0). The smaller ζ of the nonactivated SNs in neutral pH is apparently caused by the ionized OH^-, which is nonexistent in the activated SNs. The nonactivated and activated SNs had about the same ζ values at pH = 3–4, *i.e.*, ζ = 23.12 ± 2.76 mV for the former and ζ = 26.99 ± 3.40 mV for the latter, because the silica surfaces of both samples are protonated while the exposed QAC-OH in the nonactivated SNs are neutralized in the strongly acidic solution.

SNLM–PVDF. The amount of SN (m_{SN}) loaded over the coating area (A_M) of 7.55 cm^2 was ~0.6 mg, which would form a dense film thickness (δ_m) of 462 nm based on the silicalite density ρ_s ~ 1.72 g cm^{-3}, *i.e.*, $\delta_m = m_{SN}/\rho_s \cdot A_M$. However, the SNLM on the macropore PVDF surface (Fig. 2a) had a uniform

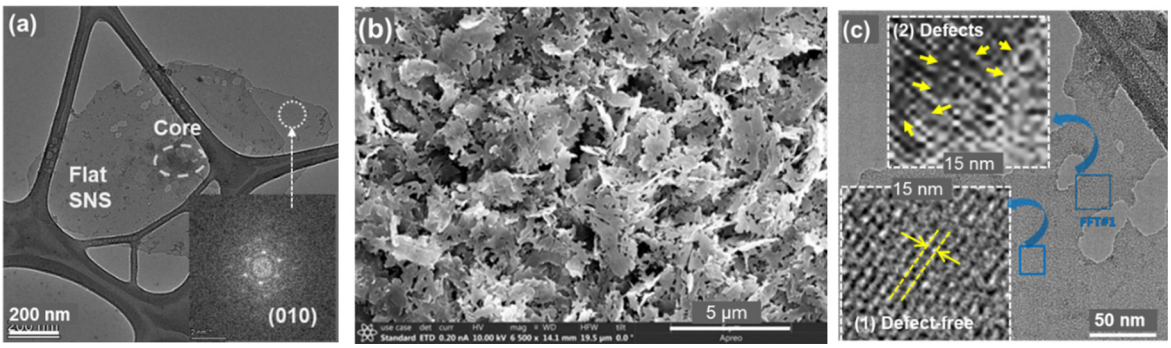

Fig. 1 The microstructure of the SNs: (a) TEM image of a typical rhombus crystal obtained by seeded secondary growth (inset: electron diffraction pattern), (b) SEM image of highly perforated flat SN flakes, and (c) HR TEM images of the SN (insets: 1 – defects-free SN surface in *a*–*c* plane and 2 – defects in edge areas).

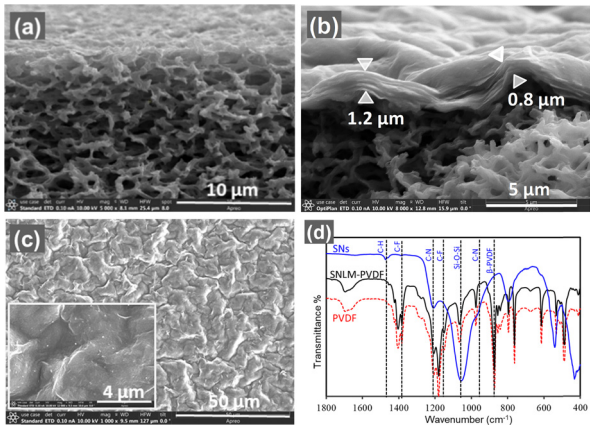

Fig. 2 The SNLM–PVDF membrane morphology: (a) the porous PVDF substrate, (b) the cross-section of the SNLM–PVDF, (c) the SNLM surface (inset: high magnification), and (d) the FTIR spectra of the SNs, PVDF, and SNLM–PVDF.

thickness (δ_m) of 1.0 ± 0.2 μm (Fig. 2b and Fig. S7a, ESI†). Thus, the SN-to-PVDF volume ratio ($V_{SN}:V_{PVDF}$) within the SNLM layer was estimated to be about 1 : 1 in dry conditions. The dry SNLM layer appeared to be wrinkled but conformed to the PVDF substrate surface without cracking (Fig. 2c) because of the mechanical flexibility of the large 4-nm-thin SNs well-aligned along the *a*–*c* plane (Fig. S8, ESI†). The FTIR spectrum of the SNLM–PVDF is apparently convolution of the SN and PVDF spectra with no appreciable sign of new chemical bonds (Fig. 2d), indicating a physically retained SNLM by the PVDF binder.[15] The SNLM–PVDF exhibited a tensile stress and a strain at break of 82.3 ± 6.0 MPa and 25.5 ± 2.5%, respectively, that were slightly improved from those of the PVDF substrate, which were 75.2 ± 5.5 MPa and 20.1 ± 3.0%, respectively (Fig. S7b, ESI†). This could be attributed to the minimal PVDF in the suspension coated on the substrate. The FAA3-50 membrane had a very small strain tolerance of ~2.5% although with a large tensile stress of >1000 MPa.

AEM ASR. In the hydrated SNLM layer, the QAC-OH groups ($\equiv N^+{\cdot}OH^-$) exposed at the SN surface defects are ionized to release exchangeable OH^- (Fig. 3a); and meanwhile, the entering and diffusion of cations (*e.g.*, K^+) through the SN/PVDF interfacial boundary may be hindered by steric effects of the positively charged (*i.e.*, $\equiv N^+$) SN surface in the boundary. The SNLM layer had a smaller conductivity ($\sigma_m = \delta_m/ASR$ = 0.14–0.21 mS cm^{-1}) than the FAA3-50 (σ_{FAA} = 7.08–8.03 mS cm^{-1}), which was consistent with literature values.[16] The small ASR of the SNLM–PVDF is a result of the SNLM thinness (δ_m ~ 1 μm) and the high conductivity of the electrolyte-filled PVDF substrate (σ_s = 54–66 mS cm^{-1}). The ASR of the SNLM–PVDF and FAA3-50 decreased when increasing the temperature (Fig. 3b) because of the activated ion transport diffusivity (D_{OH^-}). However, the temperature-dependency of ASR was more pronounced for the SNLM–PVDF than for the FAA3-50, suggesting a smaller width of the SN/PVDF boundary and a greater activation energy barrier than the water channels in the AEP. The SNLM–PVDF ASR was slightly larger at <40 °C but became smaller than the FAA3-50 at >40 °C (Fig. 3b).

The electrolyte-filled PVDF substrate had a low ASR decreasing with increasing C_{KOH}. The ASR of SNLM–PVDF was drastically lowered by over 40% when C_{KOH} increased from 5 wt% to 10 wt% (Fig. 3c), indicating that the OH^- concentration (C_{OH^-}) in SNLM increased accordingly to enhance the σ_m,[6]

$$ASR = \delta_m/\sigma_m = \delta_m \Big/ \left(z^2F^2\frac{C_{OH^-}D_{OH^-}}{RT}\right) \quad (1)$$

where z, F and D_{OH^-} are the charge of OH^-, the Faraday constant, and the OH^- transport diffusivity, respectively. The ASR of SNLM–PVDF became less sensitive to C_{KOH} > 10 wt% (Fig. 3c) likely because of increased SN surface deprotonation ($\equiv Si{-}OH + OH^- \rightarrow \equiv Si{-}O^- + H_2O$) in the extremely high C_{OH^-} that creates negatively charged surfaces to hinder the OH^- diffusion.

Water electrolysis. The SNLM–PVDF-equipped WE was first tested for alkaline WE at 60 °C using a 5 wt% KOH solution where its ARS was lower than the FAA3-50. The polarization curves (Fig. 4a) show lower operation voltages for WE with the SNLM–PVDF than that with the FAA3-50. In the 120-h WE at a current density (i_{WE}) of 400 mA cm^{-2}, the former operated at a voltage from 1.88 to 2.00 V, which was lower than the latter which operated from 1.91 to 2.20 V (Fig. 4b). The lower operation voltage of the SNLM–PVDF WE may be attributed to its smaller ASR at 60 °C (Fig. 3b) that reduced the Ohmic overpotential ($\Delta V_{ohm} = i_{WE}{\cdot}ASR_{cell}$) in WE. The SNLM–PVDF WE reached a coulombic efficiency of ~97% (CE = $A_m i_{WE}/2Fr_{H_2}$; r_{H_2} flowrate of H_2) that evidenced negligible internal current and gas crossover through the membrane. The SNLM–PVDF performance was also comparable to AEM WE with similar electrodes in the literature

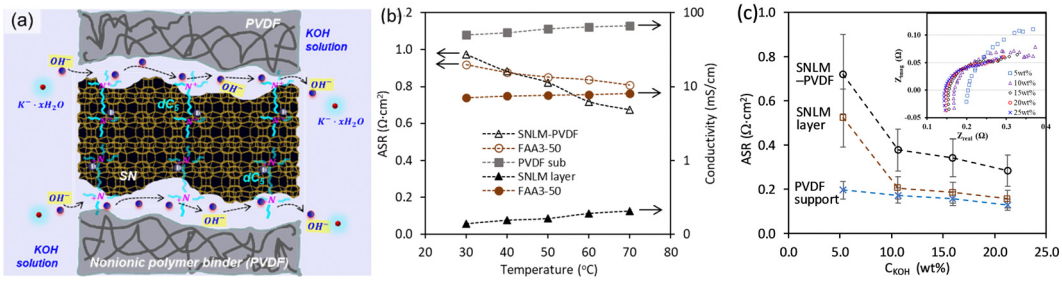

Fig. 3 (a) Depiction of the OH^- conduction mechanism in hydrated SNLM, (b) temperature-dependencies of AEM ASR and conductivity in 5 wt% KOH, and (c) ASR of SNLM–PVDF and PVDF *vs.* C_{KOH} at 60 °C (inset: EIS Nyquist spectra 1–100 kHz).

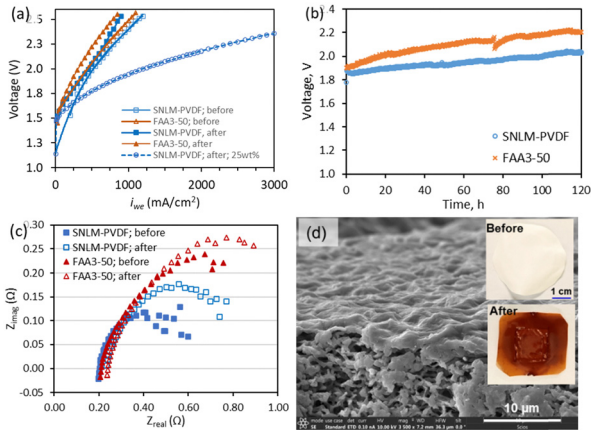

Fig. 4 (a) Polarization curves at 60 °C before and after 120 h WE operation, (b) 120-h WE at i_{WE} = 400 mA cm^{-2}, (c) EIS Nyquist spectra before and after WE operation, and (d) SEM image of the SNLM–PVDF after WE (insets: photos before and after WE).

(Table S1, ESI†). The ASR of SNLM–PVDF WE increased slightly from 0.81 to 0.94 Ω cm^2 while that of the FAA3-50 WE increased from 0.85 to 0.97 Ω cm^2 over 120 h (Fig. 4c). These small increases in cell ASR were largely reversible after resting for 4 h. A polarization curve was then measured for a 25 wt% KOH solution. The WE with SNLM–PVDF achieved remarkable i_{WE} of 1000, 2000, and 3000 mA cm^{-2} at 1.94, 2.18, and 2.35 V, respectively (Fig. 4a). The SNLM–PVDF was physically undamaged with brown coloration (Fig. 4d) after WE operations due to limited loss of –HF groups from the stable PVDF.[17] The SNLM–PVDF showed good reproducibility in WE performance (Fig. S6, ESI†).

In summary, SNs with surface QAC groups were synthesized to fabricate the SNLM–PVDF, which exhibited low ASR for anion conduction and outperformed the commercial FAA3-50 AEM in alkaline WE with lower operation voltages. The results demonstrate that the QAC-templated SNs can be a new class of building blocks for high-performing AEMs for alkaline WE. Our ongoing efforts are focused on developing unsupported SN–polymer mixed membranes with the SN surface aligned along the thickness or in house-of-cards structures to further enhance the ion conduction through the SN/polymer interfaces.

Y. S.: investigation, formal analysis, and data curation. D. S.: investigation, and data curation. Z. C.: investigation. J. G.: resources. J. D.: conceptualization, supervision, formal analysis, writing.

Research supported by the U.S. NSF Grant #CBET-1935205 and the George Rieveschl Jr. Endowment Funds.

Data availability

The data supporting this article have been included as part of the ESI.†

Conflicts of interest

There are no conflicts to declare.

References

1 (*a*) D. Henkensmeier, M. Najibah, C. Harms, J. Žitka, J. Hnát, K. Bouzek and J. Electrochem, *Energy Convers. Storage*, 2021, **18**, 024001; (*b*) Y. C. Lei, J. Zhou, W. Zhou, Y. Wang, M. Zhang, A. Zhang and L. Wang, *Chem. Commun.*, 2024, **60**, 11000.
2 (*a*) C. Santoro, A. Lavacchi, P. Mustarelli, V. Di Noto, L. Elbaz, D. R. Dekel and F. Jaouen, *ChemSusChem*, 2022, **15**, 202200027; (*b*) Y. S. Kim, *ACS Appl. Polym. Mater.*, 2021, **3**, 1250; (*c*) Z. Zakaria and S. K. Kamarudin, *Int. J. Energy Res.*, 2021, **45**, 18337.
3 (*a*) M. G. Marino and K. D. Kreuer, *ChemSusChem*, 2015, **8**, 513; (*b*) D. S. Kim, C. H. Fujimoto, M. R. Hibbs, A. Labouriau, Y. K. Choe and Y. S. Kim, *Macromolecules*, 2013, **46**, 7826; (*c*) Z. Liu, S. D. Sajjad, Y. Gao, H. Yang, J. J. Kaczur and R. I. Masel, *Int. J. Hydrogen Energy*, 2017, **42**, 29661; (*d*) K. M. Hugar, H. A. Kostalik and G. W. Coates, *J. Am. Chem. Soc.*, 2015, **137**, 8730; (*e*) Y. Zha, M. L. Disabb-miller, Z. D. Johnson, M. A. Hickner and G. N. Tew, *J. Am. Chem. Soc.*, 2012, **134**, 4493.
4 (*a*) J. Müller, A. Zhegur, U. Krewer, J. R. Varcoe and D. R. Dekel, *ACS Mater. Lett.*, 2020, **2**, 168; (*b*) P. Shirvanian, A. Loh, S. Sluijter and X. Li, *Electrochem. Commun.*, 2012, **132**, 107140.
5 Y. Zheng, U. Ash, R. P. Pandey, A. G. Ozioko, J. Ponce-González, M. Handl, T. Weissbach, J. R. Varcoe, S. Holdcroft, M. W. Liberatore, R. Hiesgen and D. R. Dekel, *Macromolecules*, 2018, **51**, 3264.
6 (*a*) Z. Xu, I. Michos, X. Wang, R. Yang, X. Gu and J. Dong, *Chem. Commun.*, 2014, **50**, 2416; (*b*) Z. Xu, I. Michos, Z. Cao, W. Jing, X. Gu, K. R. Kinkel, S. Murad and J. Dong, *J. Phys. Chem. C*, 2016, **120**, 26386.
7 (*a*) K. R. Hinkle, C. J. Jameson and S. Murad, *J. Phys. Chem. C*, 2014, **118**, 23803; (*b*) S. H. Jamali, T. J. H. Vlugt and L. C. Lin, *J. Phys. Chem. C*, 2017, **121**, 11273.
8 Y. Xia, H. Cao, F. Xu, Y. Chen, Y. Xia, D. Zhang, L. Dai, K. Qu, C. Lian, K. Huang, W. Xing, W. Jin and Z. Xu, *Nat. Sustainable*, 2022, **5**, 1080.
9 L. Iskhakova, Z. Cao, X. Sun, J. Gabski and J. Dong, *J. Membr. Sci.*, 2023, **669**, 121328.
10 M. Y. Jeon, D. Kim, P. Kumar, P. S. Lee, N. Rangnekar, P. Bai, M. Shete, B. Elyassi, H. S. Lee, K. Narasimharao, S. N. Basahel, S. Al-Thabaiti, W. Xu, H. J. Cho, E. O. Fetisov, R. Thyagarajan, R. F. Dejaco, W. Fan, K. A. Mkhoyan, J. I. Siepmann and M. Tsapatsis, *Nature*, 2017, **543**, 690.
11 Z. Cao, L. Iskhakova, X. Sun, Z. Tang and J. Dong, *ACS Appl. Nano Mater.*, 2012, **4**, 2895.
12 Z. Cao, S. Zeng, Z. Xu, A. Arvanitis, S. Yang, X. Gu and J. Dong, *Sci. Adv.*, 2018, **4**, eaau8634.
13 S. Kamali, M. Zhiani and H. Tavakol, *Renewable Energy*, 2020, **154**, 1122.
14 (*a*) G. F. Li, D. Yang and P. Y. Abel Chuang, *ACS Catal.*, 2018, **8**(12), 11688; (*b*) A. S. Pushkarev, I. V. Pushkareva, S. P. du Preez and D. G. Bessarabov, *Catalysts*, 2023, **13**(3), 554; (*c*) A. Carbone, S. C. Zignani, I. Gatto, S. Trocino and A. S. Aricò, *Int. J. Hydrogen Energy*, 2020, **45**(16), 9285; (*d*) Y. S. Park, J. Jeong, Y. Noh, M. J. Jang, J. Lee, K. H. Lee, D. C. Lim, M. H. Seo, W. B. Kim, J. Yang and S. Choi, *Appl. Catal., B*, 2021, **292**, 120170.
15 (*a*) V. Vijayakumar, T. Y. Son, K. S. Im, J. E. Chae, H. J. Kim, T. H. Kim and S. Y. Nam, *ACS Omega*, 2021, **6**, 10168; (*b*) D. Ion-Ebras, R. D. Andrei, S. Enache, S. C. C. C. Negrilă, C. Jianu, A. Enache, I. Boeras, E. Carcadea, M. Varlam, B. S. Vasile and J. Ren, *Materials*, 2021, **14**, 4952.
16 C. Lo Vecchio, A. Carbone, I. Gatto and V. Baglio, *Polymers*, 2023, **15**, 1555.
17 Y. Jin, H. Chen, G. Wen, J. Zhou, Z. Wang, F. Zhang and Z. Cui, *Eur. Polym. J.*, 2024, **207**, 112816.

